Revision 1

Incorporation of Fe^{2+} and Fe^{3+} in bridgmanite during magma ocean crystallization

Asmaa Boujibar[1,*], Nathalie Bolfan-Casanova[1], Denis Andrault[1], M. Ali Bouhifd[1], Nicolas Trcera[2]

[1] Laboratoire Magmas et Volcans, UMR-6524, Université Blaise Pascal, Clermont-Ferrand, France. [2] Synchrotron SOLEIL, Gif Sur Yvette, France

[*] Corresponding author (asmaa.boujibar@nasa.gov), now at NASA Johnson Space Center, 2101 Nasa Parkway, Houston, TX 77058, USA.

Abstract

Using large volume press, samples of bridgmanites (Bg) in equilibrium with both silicate melt and liquid Fe-alloy were synthesized in order to replicate the early period of core-mantle segregation and magma ocean crystallization. We observe that the Fe partition coefficient between Bg and silicate melt ($D_{Fe}^{Bg/melt}$) varies strongly with the degree of partial melting (F). It is close to 1 at very low F and adopts a constant value of ~0.3 for F values above 10 wt%. In the context of a partially molten mantle, a larger F (closer to liquidus) should yield Fe-depleted Bg grains floating in the liquid mantle. In contrast, a low F (closer to solidus) should yield buoyant pockets of silicate melt in the dominantly-solid mantle.

We also determined the valence state of Fe in these Bg phases using X-Ray absorption near-edge spectroscopy (XANES). Combining our results with all available data sets, we show a redox state of Fe in Bg more complex than generally accepted. Under the reducing oxygen fugacities (fO_2) of this study ranging from IW-1.5 and IW-2, the measured Fe^{3+} content of Bg is found moderate ($Fe^{3+}/\Sigma Fe = 21 \pm 4$ %) and weakly correlated with Al-content.

When fO_2 is comprised between IW-1 and IW, this ratio is correlated with both Al-content and oxygen fugacity. When fO_2 remains between IW and Re/ReO$_2$ buffers, Fe^{3+}/ΣFe ratio becomes independent of fO_2 and exclusively correlated with Al-content.

Due to the incompatibility of Fe in Bg and the variability of its partition coefficient with the degree of melting, fractional crystallization of the magma ocean can lead to important chemical heterogeneities that will be attenuated ultimately with mantle stirring. In addition, the relatively low Fe^{3+}-contents found in Bg (21 %) at the reducing conditions (IW-2) prevailing during core segregation seem contradictory with the 50 % previously suggested for the actual Earth's lower mantle. This suggests the presence of 1.7 wt% Fe^{3+} in the lower mantle, which reduces the difference with the value observed in the upper mantle (0.3 wt%). Reaching higher concentrations of trivalent Fe requires additional oxidation processes such as the late arrival of relatively oxidized material during the Earth accretion or interaction with oxidized subducting slabs.

Keywords: Bridgmanite, lower mantle, magma ocean, melting, partitioning, redox, ferric iron, XANES.

Introduction

During the process of Earth accretion, as soon as the Earth achieved about 30% of its present-day mass, the floor of the magma ocean reached a pressure sufficient to enter the stability domain of bridgmanite (Al-bearing (Mg,Fe)SiO$_3$ with perovskite-type structure, Bg). As Bg represents 80% of the mass of the lower mantle, the phase relations between Bg and melt are key parameters in understanding the early, as well as the actual, mantle dynamics. As a matter of fact, two recent studies report contradictory results on the partitioning of Fe

between Bg and melt at very high pressures, leading to an open controversy about the buoyancy of silicate melts potentially present today in the D"-layer sitting just above the core-mantle boundary (Andrault et al., 2012; Nomura et al., 2011). Concerning the early period when the Earth was partially molten, it is also unclear how bridgmanite has controlled the redox conditions during magma ocean crystallization.

It has been proposed that Al-bearing silicate Bg displays a major ability to incorporate Fe^{3+} even under reducing conditions (Lauterbach et al., 2000; McCammon, 1997). As point defects can have strong effects on the physical and chemical properties, like electrical conductivity (Xu et al., 1998), trace element partitioning (Jackson et al., 2014; Liebske et al., 2005; Walter et al., 2004) and compressibility (Andrault et al., 2007), several studies have investigated the mechanism of Fe^{3+} incorporation in Bg. The predominant mechanism of Fe^{3+} insertion in Al-$(Mg,Fe)SiO_3$ is the coupled substitution of Al for Mg and Si (Andrault et al., 2007; Frost and Langenhorst, 2002; Lauterbach et al., 2000) in their respective dodecahedral and octahedral sites.

Both the Al content and the Fe/(Fe+Mg) molar ratio of bridgmanite have been previously reported to enhance the solubility of Fe^{3+} in Bg (Frost and Langenhorst, 2002; Lauterbach et al., 2000). On the other hand, the fact that Fe^{3+} content in Al-bearing bridgmanite was found to be independent on capsule material (Re or Fe; i.e. more oxidizing or reducing conditions) suggests that the Fe^{3+} incorporation could be independent of the fO_2 (Frost et al., 2004; Frost and McCammon, 2008). This conclusion has been challenged by the report of a strong dependence of Fe^{3+} incorporation in Al-free Bg with fO_2 and nature of the capsule material (Nakajima et al., 2012). Moreover, it has been shown that with compositions equivalent to the bulk silicate Earth, the Fe^{2+} in Bg disproportionates into Fe^{3+} and Fe metal (Frost et al., 2004; Lauterbach et al., 2000). Such process implies that Bg acts as a "sink for ferric iron" (McCammon, 1997).

3

All these experimental studies were conducted in a limited range of fO_2, between 1 log unit below the iron/wüstite (IW-1) and the Re/ReO$_2$ buffer, (~IW+7, (Pownceby and O'Neill, 1994)). Such fO_2 conditions contrast sharply with the highly reducing fO_2, potentially down to IW-4, prevailing during the two major events of the early Earth differentiation: core formation and crystallization of the magma ocean (Javoy et al., 2010; Wade and Wood, 2005). The aim of this study is to investigate the incorporation of iron in Bg and its redox state during magma ocean crystallization under reducing conditions. We also report on the partitioning of major elements (Mg, Si, Fe, Al) between Bg and melt as a function of the degree of partial melting. A major question that we want to address is the role of bridgmanite crystallization on the redox state of the primitive mantle. For this, we conducted a series of experiments using a multi-anvil press at 25 GPa and temperatures comprised between the solidus and the liquidus of the silicate, and at oxygen fugacities down to IW-2. We determined the chemical compositions of the different phases using electron microprobe and the valence state of Fe using X-Ray absorption near-edge spectroscopy (XANES).

Methods

Sample syntheses

Starting compositions consist of synthetic powders with compositions close to enstatite chondrites, composed of 68 wt% silicate and 32 wt% metal, with variable S and Si contents in the metal and Al$_2$O$_3$ in the silicate (Table 1). The silicates were prepared by finely mixing dried ultra-pure oxides and carbonates (SiO$_2$, MgO, Al$_2$O$_3$, TiO$_2$, Cr$_2$O$_3$, MnO, Na$_2$CO$_3$, CaCO$_3$ and K$_2$CO$_3$). The silicate mixtures were dried and decarbonated overnight at 1000°C. The metal powders were prepared by finely mixing ultra-pure Fe, Ni, Si, FeS, Co and Mn. The starting compositions, obtained by intimately mixing the silicates and the metals, were kept in a vacuum oven to avoid hydration.

4

Our syntheses were performed using graphite capsules that transform into diamond at high-pressures and high-temperatures. This results in contamination of the metal by carbon that was estimated to vary from 6.5 to 13.3 wt% C as a function of the experimental conditions. We preferred the use of graphite compared to MgO capsule, because carbon does not react with the silicate melt, while its effect on the metal composition and thus on oxygen fugacity (see below), can be measured and calculated respectively. MgO capsule would have reacted with the silicate melt, making it impossible to infer the chemical fractionation at constant bulk composition. For instance, adding some MgO to a composition like that of enstatite chondrites yields disappearance of free SiO_2 and formation of olivine, which disables the study of the melting properties of this chondrite.

We performed experiments at 25 GPa and temperatures ranging from 1900 to 2050°C, using the Kawai-type 1500-ton multi-anvil press of the Laboratoire Magmas et Volcans (Table 2). We used tungsten carbide cubes with 4 mm truncations, Cr-doped MgO octahedra of 10 mm length as pressure media and graphite capsules. The pressure calibration was previously described by (Boujibar et al., 2014). Heating and thermal insulation of the experimental charge were ensured by a $LaCrO_3$ furnace and a ZrO_2 sleeve, respectively. To protect the samples from La and Cr contamination, MgO sleeves were placed between the furnace and the capsule. We disposed alumina cylinders on each side of the capsule to enhance the pressure. Temperature was measured in two reference experiments using an axial $W_5Re/W_{26}Re$ thermocouple up to 2300°C. For all the other experiments, we did not use any thermocouple to avoid sample contamination by W and Re. Temperature was estimated using the relationship between electrical power and temperature obtained from the thermocouple-bearing experiments.

In our experiments, we conducted fractional crystallization, rather than sample partial melting, which yielded sufficiently large crystals of Bg (Tsuruta and Takahashi, 1998). After reaching the target pressure, we heated the samples above the liquidus temperature of the silicate fraction, then cooled rapidly (in less than one minute) to the target temperature comprised

5

between the solidus and the liquidus, and maintained this temperature for 30 min to 3 h
(Supplementary Fig. 1). This plateau was obtained by maintaining the electrical power constant,
which is expected to induce a slow decrease of the temperature, due to the progressive
degradation of the furnace efficiency. By using this method, we could increase the grain size in
our charges and help segregation of the melt into pools large enough for electron probe
microanalyses. As all charges have been completely molten at some point, we avoided the
presence of relict solids, especially any metal inclusions within the Bg crystals or at their grain
boundaries.

All the experiments were performed above the liquidus of iron metal. This is
evidenced by the texture of the samples and round shape of metal blobs. Melting of pure iron
at 25 GPa, is expected at ~2200 K (Anzellini et al., 2013). However, considering the amount
of light elements (Si and C, and sometimes S) dissolved in the metal, the melting temperature
of the alloy should be a few hundred of degrees lower. At 25 GPa, the eutectic melting curve
in the Fe-C system is located at ~2000 K (1727 °C) (Lord et al., 2009), much below the
1900°C of the experiments.

Chemical analyses

Phase relations and chemical compositions (Tables 2-3 and Supplementary Table 1)
were determined using the CAMECA SX100 electron probe micro-analyzer (EPMA) of the
Laboratoire Magmas et Volcans. We used an accelerating voltage of 15 kV with a 2 to 20 μm
(defocused) electron beam. All phases were analyzed at 15 nA except the Bg that was
analyzed at 2 nA to avoid amorphization. Standards were pure metals and silicates such as
forsterite, wollastonite, corundum, albite, orthose, fayalite, $MnTiO_3$, Cr_2O_3, ZnS, Fe, Ni, Si,
Mn and Co.

6

Oxygen fugacity

We calculated the fO_2 in our samples using the equilibrium between Fe metal and the silicate melt:

$$Fe^{metal} + \tfrac{1}{2} O_2 = FeO^{silicate} \tag{1}$$

The fO_2 is estimated relative to the Fe/FeO buffer (ΔIW) following the expression:

$$\Delta IW = 2 \log \left(X_{FeO}^{sil} \gamma_{FeO}^{sil} \middle/ X_{Fe}^{met} \gamma_{Fe}^{met} \right) \tag{2}$$

where X_{FeO}^{sil} and X_{Fe}^{met} are the mole fractions of FeO in the silicate melt and Fe in the metal, respectively. The activity coefficient of Fe in the metal (γ_{Fe}^{met}) was derived from the online metal activity calculator provided by the University of Oxford (Wade et al., 2012). We considered an activity coefficient of FeO in the silicate melt (γ_{FeO}^{sil}) of 1.7, in agreement with previous experimental and thermodynamic estimations (O'Neill and Eggins, 2002). This value of γ_{FeO}^{sil} was also considered based on the previous study indicating that there is no significant pressure effect (at least up to 15 GPa) on the activity of FeO in silicate melts (Toplis, 2005).

Measurement of the redox state of iron

The valence of iron in Bg was investigated using XANES spectroscopy at LUCIA beamline of SOLEIL synchrotron, operating with a storage ring current and energy of 400 mA and 2.75 GeV, respectively. A Si(311) double-crystal monochromator was used for these measurements. Fluorescence spectra at the Fe K-edge were collected successfully with a beam size of 5x5 µm² in sample regions where different Bg phases are present; (i) the Fe-poor Bg in all analyzed samples, and (ii) the Fe-rich Bg for samples #104 and #129 (see below). Measurements were performed using the same experimental set-up as in our previous study (Boujibar et al., 2014). XANES spectra were recorded with a total counting time of 9 min

7

(corresponding to at least 3 successive acquisitions on the same sample area), at energies ranging from 7050 eV up to 7300 eV, with step resolutions of 2, 0.1, 0.2, 0.5 and 1 eV for energy ranges of 7050-7106, 7106-7120, 7120-7150, 7150-7220 and 7220-7300 eV, respectively. The location of each analytical spot on the samples was controlled by prior chemical mapping using X-ray fluorescence. As XANES standards, we used a siderite powder (with 100% $Fe^{2+}/\Sigma Fe$) and a single crystal of andradite garnet (containing 100% $Fe^{3+}/\Sigma Fe$) to calibrate respectively pre-edge characteristics of Fe^{2+} and Fe^{3+} end members in octahedral coordination. Standards of intermediate valences were a San Carlos orthopyroxene powder and a synthetic bridgmanite, which respective $Fe^{3+}/\Sigma Fe$ ratios of 5 % and 22 % were previously determined by Mössbauer measurements. The dodecahedron of Bg is so distorted that the first oxygen neighbors are close to be in octahedral coordination as shown by EXAFS measurements (Andrault et al., 1998; Farges et al., 1995) and by X-ray single crystal diffraction (Jephcoat et al., 1999).

Then, the absorption edges were normalized using Athena software (Ravel and Newville, 2005). The resulting normalized spectra of Bg show two main features located close to the absorption edge (Fig. 1), similar to our Bg standard and to previous spectra (see (Andrault et al., 1998)). The pre-edge features were modeled using Peak-Fit Package (Jandel Scientific) between 7106 and 7120 eV using two peak-components with a fixed band width of 1.65 eV and a 50:50 Lorentz/Gaussian peak shape. Due to the limited energy resolution, only two components were extracted, instead of the three previously found for the Fe^{2+} in octahedral coordination (Bolfan-Casanova et al., 2012; Wilke et al., 2001). An example of pre-edge fitting is shown in Supplementary Figure 2. The results of fitting for standards and samples are shown in Table 3. The centroid of each spectrum is calculated by summing each peak position weighted by its corresponding area fraction (see Supplementary Fig. 2). The resulting pre-edge centroid energy is calculated by averaging the centroids measured on

8

different grains (Fig. 2). The centroid position of the pre-edge of the standards are used to perform a standardization of $Fe^{3+}/\Sigma Fe$ as a function of the centroid position, in a similar way as Wilke et al. (2001) and Bolfan-Casanova et al. (2012), see Fig. 3. We used this calibration line to determine the Fe^{3+} content of our synthetic bridgmanites. The maximum uncertainty in standardization is 10% $Fe^{3+}/\Sigma Fe$ (as seen in Fig. 3). This estimation is based on errors in determining the centroid position of the standards, in particular for andradite single crystal, which centroid position varies with orientation relative to the X-ray beam. In contrast, the standard deviation of the centroid position for the Bg phase, based on 8 different measurements performed on the Bg standard, is significantly lower than for andradite, due to a lower observed anisotropy of absorption.

Results and discussion

Samples textures

Our run products generally contain a liquid metal, silicate melt, stishovite and bridgmanites (Fig. 4). Additional features specific to each experiment are the presence of (i) majorite in sample #103, caused by a slightly lower pressure in this experiment, (ii) liebermannite (K-hollandite) in sample #104 that is the solidus phase for our starting material, (iii) a single Bg phase (see below) and absence of stishovite for the Al-free sample (#122), which presents a higher degree of partial melting (69% of melting, as indicated by mass balance) than other samples. The partitioning of K over Na in liebermannite is very pronounced (15.16 wt% K_2O and 0.95 wt% Na_2O). Detailed compositions of the coexisting phases and the phase proportions (determined by mass balance calculations) are presented in Supplementary Table 1.

Sample #103 shows domains of majoritic garnet and Fe-poor bridgmanite embedded in each other (Fig. 4e), suggesting the simultaneous crystallization of both phases. In sample #122, the silicate melt and bridgmanite are the only observed phases (stishovite is not found in the experimental charge) (Fig. 4d), suggesting the early crystallization of bridgmanite, just after the experimental temperature is reduced below the liquidus. Based on these observations, the likely sequence of phase crystallization for the enstatite chondrite composition is: bridgmanite (and/or majorite at pressures lower than 25 GPa), stishovite then liebermannite (K-hollandite).

Phase relations and Bg-melt partitioning

All samples are characterized by the presence of two different Bg phases, except sample #122 (Fig. 4d): a first Bg phase (Bg1) is present as large grains with Fe# (100*Fe/(Fe+Mg)) of 1.7 to 2.4, being relatively depleted in Fe compared to a second one (Bg2) located at the grain boundaries with a much higher Fe# up to 4.3 (Table 3). Both Bg phases present homogeneous chemical compositions and no significant chemical zoning. We note that similar type of biphasic composition is observed in magmatic terrestrial and martian olivines (Ennis and McSween, 2014; Milman-Barris et al., 2008; Welsch et al., 2012), with rims enriched in incompatible elements surrounding relatively depleted cores. The presence of two different Bg phases in our samples denotes two steps of Bg crystallization from the melt in the course of our experiments: the abundant Fe-depleted Bg grains recorded the Bg-melt equilibrium when crossing the liquidus temperature (Supplementary Fig. 1). The Fe-enriched Bg rims crystallized at lower temperature on the plateau, when the furnace power was maintained constant for 1 to 3 hours.

For the Fe-rich Bg phase (Bg2), the solid-liquid partition coefficients can be directly derived from chemical analyses of this Bg and the observed melt (Supplementary Table 1). In

10

the case of Fe-poor Bg phase (Bg1), we need to retrieve the composition of the silicate melt

from which the Bg1 grains crystallized at equilibrium. This primary liquid includes the "final"

observed melt, as well as the "secondary" Bg2 and the other minor phases (e.g. liebermannite)

that all crystallized later on the course of the experiments. The chemical composition of the

primary melt can be calculated from the different components cited above, with all phases

compositions weighted by their mass fractions in the sample (Supplementary Table 2). For

sample #103, we did not include the majorite phase in the calculations of the melt

composition, as the sample texture suggests that this phase crystallized simultaneously to

Bg1. In all cases, the degree of partial melting (F) of the silicate fraction of the sample is

determined from classical mass balance calculations (Albarède and Provost, 1977) (see Table

2).

The partitioning of Fe, Al, Mg and Si between bridgmanite and melt ($D_i = C_i^{Bg} / C_i^{melt}$

with C_i the concentration in wt% of the element i) are calculated and plotted as a function of F

(Fig. 5). The F values reported in Figure 5 correspond either to the fractions of silicate melt

directly observed through the sample texture and composition (represented by filled squares

in Fig. 5), or to the primary degree of melting (open squares), calculated by adding up the

fractions of each phases crystallized after the Bg1 grains. The value of $D_{Si}^{Bg/melt}$ appears

independent of F (at 1.1 +/- 0.1), whereas the other three elements show a plateau only for F

values above 10-40%. More precisely, $D_{Fe}^{Bg/melt} = 0.3$ +/- 0.1, $D_{Al}^{Bg/melt} = 0.7$ +/- 0.2 and

$D_{Mg}^{Bg/melt} = 1.1$ +/- 0.1, for F above ~10%, ~20% and ~40%, respectively. With decreasing the

degree of partial melting, the Bg/melt Fe, Al and Mg partition coefficients increase

significantly, attesting a much higher compatibility with the Bg-lattice. Close to the solidus

temperature (for infinitely low F value), the partitioning coefficients are all above 1; $D_{Fe}^{Bg/melt}$

= 1.1 +/- 0.1, $D_{Al}^{Bg/melt} = 1.1$ +/- 0.2, $D_{Mg}^{Bg/melt} = 1.7$ +/- 0.1 and $D_{Si}^{Bg/melt} = 1.1$ +/- 0.1, which

denotes the fact that the major and minor incompatible elements in this case are restricted to Ca, Na, and K. The change with F of partition coefficients for Ca, Na, K, Mn, Ti, and Cr are shown in Supplementary Figure 3. Major observed features for these elements are: (1) the incompatibility of Ca, Na and K in Bg, (2) the very similar behavior of Mn and Fe and (3) the compatibility then incompatibility of Cr at F<7 and above this F-value respectively.

At the experimental pressure of about 25 GPa, we thus find that Fe and Al behaviors change from compatible ($D_{Fe}^{Bg/melt} = D_{Al}^{Bg/melt} = 1.1$) to largely incompatible ($D_{Fe}^{Bg/melt} = 0.3$ and $D_{Al}^{Bg/melt} = 0.7$) with increasing the degree of partial melting, whereas Mg and Si stay compatible at all temperatures. This observation is in agreement with the fact that the $MgSiO_3$ end-member is the most refractory phase since Fe and Al are preferentially partitioned into the liquid with increasing temperature. This result could explain a recent controversy about the Fe-partitioning between Bg and silicate melt at P-T conditions of the lowermost mantle. The lower $D_{Fe}^{Bg/melt}$ value of 0.2-0.3 (Nomura et al., 2011) or higher value of 0.5-0.6 (Andrault et al., 2012) could be due to a difference in the experimental temperature, closer to liquidus or solidus, respectively.

Incorporation of Fe^{3+} in bridgmanite

Three physical parameters control the redox state of Bg: the Fe number (Fe# = Fe/(Fe+Mg)), the $Fe^{3+}/\Sigma Fe$ ratio, and the Fe^{3+} content per formula unit (Fe^{3+}-pfu). Each parameter can vary with sample composition and experimental conditions:

(i) The Fe# can be determined using the electron microprobe analyses. It is intrinsically linked to the fO_2 when the Bg phase coexists with a metallic Fe-alloy, through the equilibrium FeO ⇔ Fe + 1/2 O_2. In the absence of a metallic Fe-alloy, the Fe# in Bg is much less dependent on the fO_2 and its value becomes mostly constrained by the initial sample

12

composition and by Fe^{2+} and Fe^{3+} partitioning between Bg and other oxide phases (such as ferropericlase in the lower mantle, (Wood and Rubie, 1996)). Absence of a metallic phase can occur at a fO_2 sufficiently higher than the IW buffer and in the context of Earth's formation after the segregation of the core is completed.

(ii) The $Fe^{3+}/\Sigma Fe$ ratio can be determined by XANES or Mössbauer measurements. The $Fe^{3+}/\Sigma Fe$ ratio is very likely linked to the fO_2, in a comparable manner than for any oxide phase. For Bg, this ratio is also strongly dependent on the Al-content, due to the well-known strong Fe^{3+}-Al^{3+} coupling (see below). Figure 6 shows the effect of Fe# on $Fe^{3+}/\Sigma Fe$. Below IW buffer, the silicate is Fe-depleted, and fO_2 and Fe# are correlated. Therefore, we plot the $Fe^{3+}/\Sigma Fe$ ratio as a function of Fe# for experiments equilibrated at a fO_2 higher that IW (Fig. 6), in order to examine the effect of Fe# independently from the fO_2. Figure 6 shows that there is no intrinsic structural control of the $Fe^{3+}/\Sigma Fe$ ratio by the Fe# since no clear trend can be noticed. While the $Fe^{3+}/\Sigma Fe$ ratios in our samples remain comprised between 14 and 25 %, ratios in previous studies range over a much broader interval from 11 to 82 %, and up to 100% when the starting material contains exclusively Fe_2O_3 (Andrault and Bolfan-Casanova, 2001; Hummer and Fei, 2012).

(iii) the Fe^{3+}-pfu can be calculated using the $Fe^{3+}/\Sigma Fe$ ratio and the bulk Fe content (Table 3), and it can also be approximated using Fe# parameter with the relation:

$$Fe^{3+}\text{-pfu} \approx (Fe^{3+}/\Sigma Fe)*Fe\# \tag{3}$$

We report the Fe^{3+}-pfu as a function of the Fe#, for Al-free (Fig. 7a) and Al-bearing bridgmanites (Fig. 7b), for our samples together with a number of previous studies (Frost and Langenhorst, 2002; Frost et al., 2004; Hummer and Fei, 2012; Lauterbach et al., 2000; McCammon et al., 2004; Saikia et al., 2009; Terasaki et al., 2007). We confirm the correlation already pointed out previously between Fe^{3+}-pfu and Fe# for Bg (Frost et al., 2004), as well as

13

for other mantle phases such as ferropericlase (Jacobsen et al., 2002) and wadsleyite (Bolfan-Casanova et al., 2012; Frost and McCammon, 2009).

Previous studies based on Bg phases synthesized at relatively oxidizing conditions reported a major correlation between the $Fe^{3+}/\Sigma Fe$ and the Al-content (Frost and Langenhorst, 2002; Lauterbach et al., 2000) (Fig. 8a). Interestingly, it appears that this correlation does not apply to our samples synthesized at reducing fO_2 conditions between IW-1.5 to -2. Instead, they show a weak variation of $Fe^{3+}/\Sigma Fe$ that remains at $21 \pm 4\%$ (Fig. 8a). When reporting the Fe^{3+}-pfu in the Bg as a function of Al-pfu, we observe an increased incorporation of Fe^{3+} (pfu) with increasing Fe# as already pointed out by (Nakajima et al., 2012) (Fig. 8b). At Fe# below ~0.09 (i.e. for Bg synthesized in reducing conditions), there is a weak correlation between Fe^{3+}-pfu and the Al content in Bg. At higher Fe#, we observe an increase of Fe^{3+}-pfu with increasing Al content at a constant Fe#, especially for Al-contents above 0.05 pfu.

We finally draw a schematic evolution of the $Fe^{3+}/\Sigma Fe$ ratio as a function of the fO_2. For previous experiments, we recalculated the fO_2 from the equilibria between liquid metal and silicate melt (see (Liebske, 2005; Liebske et al., 2005) for experiments of (Frost et al., 2004)), as performed for our samples. Alternatively, for previous reports that do not contain any silicate melt (Terasaki et al., 2007), the fO_2 was estimated solely from the O content in liquid metal using empirical relationships between O content of metal, P, T and fO_2 from (Ricolleau et al., 2011). Due to the lack of precise fO_2-calibrant in some previous studies, we assumed that fO_2 is increasing progressively from IW-2 to the Fe_3O_4-Fe_2O_3 (HM) buffer, when using metallic capsules of Fe, Re, Pt or Au, and when the experiments contained both Re and ReO_2. It appears a general increase of the $Fe^{3+}/\Sigma Fe$ ratio with fO_2, in agreement with a previous report (Nakajima et al., 2012) (Fig. 9). However, the $Fe^{3+}/\Sigma Fe$ values are spread out

14

between 10 and 82 % for fO_2 conditions intermediate between the IW-2 and HM buffers.

Drawing contours for constant Al-contents suggests that:

(i)   At IW-2 the $Fe^{3+}/\Sigma Fe$ ratio is independent of the Al-content,

(ii)   Between IW-1.5 and IW-1, the $Fe^{3+}/\Sigma Fe$ ratio increases rapidly with the fO_2 for Bg-phases with an Al-content higher than 0.1 pfu,

(iii)   The $Fe^{3+}/\Sigma Fe$ ratio is weakly correlated with the fO_2 in samples with low Al-content (<0.05 pfu) for fO_2 below the Re/ReO_2 buffer,

(iv)   When fO_2 is comprised between IW-1 and IW and when the Al-content in Bg is higher than 0.05, this ratio is correlated with both Al-content and oxygen fugacity,

(v)   When fO_2 remains between IW and the Re/ReO_2 buffers, $Fe^{3+}/\Sigma Fe$ ratio becomes independent of fO_2 and exclusively correlated with Al-content,

(vi)   The $Fe^{3+}/\Sigma Fe$ ratio increases significantly with the fO_2 at conditions more oxidizing that the Re/ReO_2 buffer, especially for low Al-contents.

As shown in Fig. 9, the Fe^{3+} content of Bg is dependent on the fO_2, when fO_2 is lower than IW buffer and higher than Re/ReO_2 buffer. Unfortunately, in these ranges of fO_2, there is a too limited amount of available samples with calculated fO_2 for each Al-content, to derive a quantitative model predicting the Fe^{3+} content of Bg. On the other hand, in the intermediate range of fO_2 where experiments are conducted with Fe, Re, Pt or Au metal capsules, Fe^{3+} in Bg is only a function of Al-content. We can therefore derive a linear relationship predicting Fe^{3+} content in Bg in this intermediate range of fO_2, by neglecting the fO_2 parameter:

$$Fe^{3+}/\Sigma Fe = 336.93 * X_{Al} + 22.356 \qquad (4)$$

Where $Fe^{3+}/\Sigma Fe$ is expressed in % and X_{Al} represents the Al-content per formula unit in Bg.

Figure 10 shows the quality of the fit and the associated σ error, corresponding to 8%

15

$Fe^{3+}/\Sigma Fe$. Increasing the experimental database in the P-T conditions of the magma ocean, while accurately determining the fO_2, would help further predicting Fe^{3+} content in bridgmanite, especially with experimental fO_2 lower than IW buffer and higher than Re/ReO_2 buffer.

Implications for the crystallization of the magma ocean

Primordial chemical stratification in a crystallizing magma ocean

Several heat sources contributed to melting of the Earth's mantle during planetary differentiation, including radionuclides decay, kinetic energy supplied by impacts and gravitational energy released by core segregation. The resulting heat is partitioned between core and mantle, which depends strongly on the rheology of the planet and on the segregation mechanisms (Monteux et al., 2013). If enough heat is transferred into the mantle, partial melting could have occurred deep below the bottom of a magma ocean. However, the distribution of siderophile elements between mantle and core indicate that at the final stages of the Earth's accretion, core–mantle equilibration occurred at pressures between 40 and 60 GPa, which correspond to a base of the magma ocean located at half the depth of core–mantle boundary (Bouhifd and Jephcoat, 2011; Li and Agee, 1996b; Siebert et al., 2012). In addition, by the end of the Earth's differentiation, the Earth's core and mantle are usually assumed to have equilibrated at a fO_2 of IW-2. This fO_2 results from the present-day FeO content of the mantle (8 wt%) measured in mantle xenoliths and from the 85 wt% Fe of the core that is estimated from knowledge of the Earth's core density deficit (McDonough and Sun, 1995; Poirier, 1994). This concentration of 8 wt% FeO is usually attributed to the whole mantle, assuming a chemically homogeneous mantle. However, the primitive mantle could have been chemically stratified, due to the early crystallization of Bg.

16

If the homogeneous value of 8 wt% FeO measured in mantle xenoliths represents the bulk Earth's mantle composition, the crystallization of Bg from the primitive mantle containing a bulk FeO of 8 wt% could result in a magma ocean containing much more FeO than that. For a fraction of 50% of the BSE being crystallized, mass balance calculations (using $D_{Fe}^{Bg/melt}$ ~0.3) yield FeO-contents in the residual magma ocean and solid mantle bridgmanite of ~12 wt% and 4 wt% FeO, respectively. This fraction of half the mantle mass being crystallized is derived from the depth of the magma ocean's floor where metal and silicate equilibrated, as constrained by the core-mantle distribution of siderophile elements (Bouhifd and Jephcoat, 2011; Li and Agee, 1996a; Siebert et al., 2012).

Alternatively, if we consider that the chemical composition of xenoliths is only representative of the upper part of the mantle, the observed 8 wt% FeO could correspond to the composition of the latest Fe-enriched magma ocean. Then, using a partition coefficient $D_{Fe}^{Bg/melt}$ ~0.3 suggests that the underlying solid mantle should contain 2.4 wt% FeO. This would result in a bulk mantle FeO value of ~5.2 wt%. In both cases, due to a $D_{Fe}^{Bg/melt}$ value significantly different than 1, efficient mantle stirring would be needed to erase the chemical stratification induced by the Bg crystallization in the early magma ocean. Ultimately, 100% of the magma ocean will have recrystallized, but these values can serve to set the end members of FeO-content for the primitive mantle that mantle dynamics will tend to homogenize. We note that several geochemical and geophysical arguments were advanced to suggest the remaining presence of unmixed and primordial material in the deep mantle (Davaille, 1999; Farnetani and Samuel, 2005; Kellogg et al., 1999; Murakami et al., 2007). If these regions correspond to the solid or liquid fraction of the partially molten mantle, then their Fe-content would be lower or higher than 8 wt% Fe respectively.

Two other effects could induce heterogeneities in the mantle FeO-contents: (i) upon cooling, the progression of the crystallization front toward the planetary surface is expected to

17

induce an enrichment in FeO of the melt, which in turn should induce a FeO-gradient in the crystallizing mantle with increasing content toward the surface. (ii) Another source of heterogeneity can be the variation of the $D_{Fe}^{Bg/melt}$ partition coefficient with the degree of partial melting. Our results show that with decreasing the degree of melting, Fe becomes compatible with a $D_{Fe}^{Bg/melt}$ partition coefficient increasing up to 1.1. As partial melting can extend to high mantle depths (Andrault et al., 2011; Miller et al., 1991), the primitive mantle should have experienced a wide range of degrees of melting. It should result in a variable FeO-content in the Bg phase in equilibrium with the melt. In addition, due to a larger slope for the mantle melting curves (dT/dP) compared to the adiabatic temperature profiles, higher mantle depth should correspond to lower degree of partial melting (see (Andrault et al., 2011)). Thus, higher mantle depths are likely to involve higher $D_{Fe}^{Bg/melt}$ partition coefficients, i.e. more FeO-content in the Bg, and thus a more buoyant residual melt. In addition, the Fe^{2+} intermediate-spin to low-spin crossover in Bg at very high pressure can even enhance the partitioning of Fe into Bg (Prescher et al., 2014).

Effect of Bg crystallization on the fO_2 of the magma ocean

The mantle content of siderophile elements indicates that about half of the mantle's mass was crystallized when core-mantle segregation occurred (Bouhifd and Jephcoat, 2011; Siebert et al., 2012). This corresponds to a significant amount of bridgmanite crystallization. Thus, one should expect a FeO enrichment of the residual melt (see above). If droplets of metallic Fe-alloy are still present and in equilibrium with the magma ocean, the high FeO-content of the magma ocean should naturally induce an increase in oxygen fugacity during the Earth's accretion (following Eq. 1), potentially up to IW-2, in agreement with previous fO_2 models (Rubie et al., 2011; Wade and Wood, 2005).

18

If fractional crystallization of Bg occurs from the magma ocean after core segregation, i.e. without the presence of Fe-metal, then the situation is different. The oxygen fugacity does not depend any longer on the FeO content of the silicate. The Bg-phases synthesized here at ~IW-2 contain a moderate $Fe^{3+}/\Sigma Fe$ ratio of 21±4%, which corresponds to ~0.5 Fe^{3+} pfu. It is not much, but their crystallization should withdraw ferric iron from the melt, and hence should lead to a reduction of iron in the silicate melt. This could induce a decrease of the melt's fO_2, even if its Fe# is eventually increased.

Finally, we note that the $Fe^{3+}/\Sigma Fe$ value of 21% observed for Bg here for an fO_2 of ~IW-2 is significantly lower than the 50% previously suggested for the present-day pyrolitic lower mantle, based on more oxidizing experimental conditions (Frost and McCammon, 2008). Using the value of 21 % $Fe^{3+}/\Sigma Fe$ established at the end of core-mantle segregation, the resulting concentration of Fe^{3+} in the lower mantle becomes 1.7 wt%, which reduces the difference with the Fe^{3+}-content measured in the upper mantle (0.3 wt%) (Frost et al., 2004; McCammon, 2005). Achieving higher levels of Fe^{3+} would require additional processes such as the late accretion of relatively oxidized meteoritic material, or mantle oxidation by subduction of oxidized slabs throughout geological times.

Acknowledgements

References

Albarède, F., and Provost, A. (1977) Petrological and geochemical mass-balance equations: an algorithm for least-square fitting and general error analysis. Computers and Geosciences, 3(2), 309-326.

Andrault, D., and Bolfan-Casanova, N. (2001) High pressure phase transformations in the $MgFe_2SiO_4$ and Fe_2O_3-$MgSiO_3$ systems. Physics and Chemistry of Minerals, 28, 211-217.

Andrault, D., Bolfan-Casanova, N., Bouhifd, M.A., Guignot, N., and Kawamoto, T. (2007) The role of Al-defects on the equation of state of Al-$(Mg,Fe)SiO_3$ perovskite. Earth and Planetary Science Letters, 263, 167-179.

Andrault, D., Bolfan-Casanova, N., Lo Nigro, G., Bouhifd, M.A., Garbarino, G., and Mezouar, M. (2011) Melting curve of the deep mantle applied to properties of early magma ocean and actual core-mantle boundary. Earth and Planetary Science Letters, 304, 251-259.

Andrault, D., Lo Nigro, G., Petitgirard, S., Devidal, J.L., Veronesi, G., Garbarino, G., and Mezouar, M. (2012) Solid-liquid iron partitioning in the deep Earth's mantle. Nature, 487, 354-357.

Andrault, D., Neuville, D., Flank, A.M., and Wang, Y. (1998) Cation coordination sites in Al-$MgSiO_3$ perovskite. American Mineralogist, 83, 1045-1053.

Anzellini, S., Dewaele, A., Mezouar, M., Loubeyre, P., and Morard, G. (2013) Melting of iron at Earth's inner core boundary based on fast X-ray diffraction. Science, 26(6131), 464-466.

Bolfan-Casanova, N., Muñoz, M., McCammon, C., Deloule, E., Férot, A., Demouchy, S., France, L., Andrault, D., and Pascarelli, S. (2012) Ferric iron and water incorporation in wadsleyite under hydrous and oxidizing conditions: a XANES, Mössbauer, and SIMS study. American Mineralogist, 97, 1483-1493.

Bouhifd, M.A., and Jephcoat, A.P. (2011) Convergence of Ni and Co metal-silicate partition coefficients in the deep magma-ocean and coupled silicon-oxygen solubility in iron melts at high pressures. Earth and Planetary Science Letters, 307(3-4), 341-348.

Boujibar, A., Andrault, D., Bouhifd, M.A., Bolfan-Casanova, N., Devidal, J.-L., and Trcera, N. (2014) Metal–silicate partitioning of sulphur, new experimental and thermodynamic constraints on planetary accretion. Earth and Planetary Science Letters, 391(0), 42-54.

Davaille, A. (1999) A simultaneous generation of hotpots and superswells by convection in a heterogeneous planetary mantle. Nature, 402, 756-760.

Ennis, M.E., and McSween, H.Y. (2014) Crystallization kinetics of olivine-phyric shergottites. Meteoritics & Planetary Science, 49(8), 1440-1455.

Farges, F., Guyot, F., Andrault, D., and Wang, Y. (1995) Local structure around Fe in $Mg_{0.9}Fe_{0.1}SiO_3$: An X-ray absorption spectroscopy study at Fe-K edge. European Journal of Mineralogy, 6, 303-312.

Farnetani, C.G., and Samuel, H. (2005) Beyond the thermal plume paradigm. Geophysical Research Letters, 32(7).

Frost, D.J., and Langenhorst, F. (2002) The effect of Al_2O_3 on Fe-Mg partitioning between magnesiowüstite and magnesium silicate perovskite. Earth & Planetary Science Letters, 199, 227-241.

Frost, D.J., Liebske, C., Langenhorst, F., McCammon, C.A., Tronnes, R.G., and Rubie, D.C. (2004) Experimental evidence for the existence of iron-rich metal in the Earth's lower mantle. Nature, 428, 409-412.

21

Frost, D.J., and McCammon, C.A. (2008) The redox state of Earth's mantle. Annual Review of Earth and Planeary Science, 36, 389-420.

Frost, D.J., and McCammon, C.A. (2009) The effect of oxygen fugacity on the olivine to wadsleyite transformation: Implications for remote sensing of mantle redox state at the 410 km seismic discontinuity. American Mineralogist, 94(7), 872-882.

Hummer, D.R., and Fei, Y. (2012) Synthesis and crystal chemistry of Fe^{3+}-bearing (Mg, Fe^{3+})(Si,Fe^{3+})O_3 perovskite. American Mineralogist, 97, 1915-1921.

Jackson, C.R.M., Ziegler, L.B., Zhang, H., Jackson, M.G., and Stegman, D.R. (2014) A geochemical evaluation of potential magma ocean dynamics using a parameterized model for perovskite crystallization. Earth and Planetary Science Letters, 392(0), 154-165.

Jacobsen, S.D., Reichmann, H.J., Spetzler, H.A., Mackwell, S.J., Smyth, J.R., Angel, R.J., and McCammon, C.A. (2002) Structure and elasticity of single-crystal (Mg,Fe)O and a new method of generating shear waves for gigahertz ultrasonic interferometry. Journal of Geophysical Research-Solid Earth, 107(B2).

Javoy, M., Kaminski, E., Guyot, F., Andrault, D., Sanloup, C., Moreira, M., Labrosse, S., Jambon, A., Agrinier, P., Davaille, A., and Jaupart, C. (2010) The chemical composition of the Earth : Enstatite chondrite models. Earth and Planetary Science Letters, 293(3-4), 259-268.

Jephcoat, A.P., Hriljac, J.A., McCammon, C.A., O'Neill, H.S.C., Rubie, D.C., and Finger, L.W. (1999) High resolution synchrotron X-ray powder diffraction and Rietveld structure refinement of two (Mg,Fe)SiO_3 perovskite samples synthesized under different oxygen fugacity conditions. American Mineralogist, 84, 214-220.

Kellogg, L.H., Hager, B.H., and van der Hilst, R.D. (1999) Compositional Stratification in the Deep Mantle. Science, 283, 1881-1884.

Lauterbach, S., McCammon, C.A., van Aken, P., Langenhorst, F., and Seifert, F. (2000) Mössbauer and ELNES spectroscopy of (Mg,Fe)(Si,Al)O3 perovskite: a highly oxidized component of the lower mantle. Contributions to Mineralogy and Petrology, 138, 17-26.

Li, J., and Agee, C.B. (1996a) Geochemistry of mantle-core differentiation at high pressure. Nature, 381, 686-689.

Li, J., and Agee, C.B. (1996b) Geochemistry of mantle-core differentiation at high pressure. Nature, 381(6584), 686-689.

Liebske, C. (2005) Mantle melting at high pressure -Experimental constraints on magma ocean differentiation. Bayerishes GeoInstitut, p. 220. University of Bayreuth, Bayreuth.

Liebske, C., Corgne, A., Frost, D.J., Rubie, D.C., and Wood, B.J. (2005) Compositional effects on element partitioning between Mg-silicate perovskite and silicate melts. Contributions to Mineralogy and Petrology, 149(113-128).

Lord, O.T., Walter, M.J., Dasgupta, R., Walker, D., and Clark, S.M. (2009) Melting in the Fe-C system to 70 GPa. Earth and Planetary Science Letters, 284, 157-167.

McCammon, C. (2005) The paradox of mantle redox. Science, 308, 807-808.

McCammon, C.A. (1997) Perovskite as a possible sink for ferric iron in the lower mantle. Nature, 387, 694-696.

McCammon, C.A., Lauterbach, S., Seifert, F., Langenhorst, F., and van Aken, P.A. (2004) Iron oxidation state in lower mantle mineral assemblages. I. Empirical relations derived from high-pressure experiments. Earth & Planetary Science Letters, 222, 435-449.

McDonough, W.F., and Sun, S.S. (1995) The composition of the Earth. Chemical Geology, 120, 223-253.

Miller, G.H., Stolper, E.M., and Ahrens, T.J. (1991) The Equation of State of a Molten Komatiite 2. Application to Komatiite Petrogenesis and the Hadean Mantle. Journal of Geophysical Research, 96(B7), 11,849-11,864.

Milman-Barris, M., Beckett, J., Baker, M., Hofmann, A., Morgan, Z., Crowley, M., Vielzeuf, D., and Stolper, E. (2008) Zoning of phosphorus in igneous olivine. Contributions to Mineralogy and Petrology, 155, 739-765.

Monteux, J., Jellinek, A.M., and Johnson, C.L. (2013) Dynamics of core merging after a mega-impact with applications to Mars' early dynamo. Icarus, 226(1), 20-32.

Murakami, M., Sinogeikin, S.V., Hellwig, H., Bass, J.D., and Li, J. (2007) Sound velocity of MgSiO3 perovskite to Mbar pressure. Earth and Planetary Science Letters, 256(1–2), 47-54.

Nakajima, Y., Frost, D.J., and Rubie, D.C. (2012) Ferrous iron partitioning between magnesium silicate perovskite and ferropericlase and the composition of perovskite in the Earth's lower mantle. Journal of Geophysical Research, 117, 1-12.

Nomura, R., Ozawa, H., Tateno, S., Hirose, K., Hernlund, J.W., Muto, S., Ishii, H., and Hiraoka, N. (2011) Spin crossover and iron-rich silicate melt in the Earth's deep mantle. Nature, 473(7346), 199-202.

O'Neill, H.S.C., and Eggins, S.M. (2002) The effect of melt composition on trace element partitioning: an experimental investigation of the activity coefficients of FeO, NiO, CoO, MoO2 and MoO3 in silicate melts. Chemical Geology, 186(1–2), 151-181.

Poirier, J.P. (1994) Light elements in the Earth's outer core: A critical review. Physics of the Earth and Planetary Interiors, 85, 319-337.

Pownceby, M.I., and O'Neill, H.S.C. (1994) Thermodynamic data from redox reactions of high temperatures: IV, calibration of the Re-ReO2 oxygen buffer from EMF and niO+Ni-Pd redox sensor measurements. Contributions to Mineralogy and Petrology, 118, 130-136.

Prescher, C., Langenhorst, F., Dubrovinsky, L.S., Prakapenka, V.B., and Miyajima, N. (2014) The effect of Fe spin crossovers on its partitioning behavior and oxidation state in a pyrolotic Earth's lower mantle system. Earth & Planetary Science Letters, 399, 86-91.

Ravel, B., and Newville, M. (2005) ATHENA, ARTEMIS, HEPHAESTUS: data analysis for X-ray absorption spectroscopy using IFEFFIT. Journal of Synchrotron Radiation, 12(4), 537-541.

Ricolleau, A., Fei, Y., Corgne, A., Siebert, J., and Badro, J. (2011) Oxygen and silicon contents of Earth's core from high pressure metal–silicate partitioning experiments. Earth & Planetary Science Letters, 310, 409-421.

Rubie, D.C., Frost, D.J., Mann, U., Asahara, Y., Nimmo, F., Tsuno, K., Kegler, P., Holzheid, A., and Palme, H. (2011) Heterogeneous accretion, composition and core-mantle differentiation of the Earth. Earth & Planetary Science Letters, 301, 31-42.

Saikia, A., Boffa Ballaran, T., and Frost, D.J. (2009) The effect of Fe and Al substitution on the compressibility of MgSiO$_3$-perovskite determined through single-crystal X-ray diffraction. Physics of the Earth and Planetary Interiors, 173, 153-161.

Siebert, J., Badro, J., Antonangeli, D., and Ryerson, F.J. (2012) Metal-silicate partitioning of Ni and Co in a deep magma ocean. Earth & Planetary Science Letters, 321-322, 189-197.

Terasaki, H., Frost, D.J., Rubie, D.C., and Langenhorst, F. (2007) Interconnectivity of Fe–O–S liquid in polycrystalline silicate perovskite at lower mantle conditions. Physics of the Earth and Planetary Interiors, 161, 170-176.

Toplis, M., J. (2005) The thermodynamics of iron and magnesium partitioning between olivine and liquid: criteria for assessing and predicting equilibrium in natural and experimental systems. Contrib. Mineral. Petrol., 149, 22-39.

Tsuruta, K., and Takahashi, E. (1998) Melting study of an alkali basalt JB-1 up to 12.5 GPa: behavior of potassium in the deep mantle. Physics of the Earth and Planetary Interiors, 107, 119-130.

Wade, J., and Wood, B.J. (2005) Core formation and the oxidation state of the Earth. Earth and Planetary Science Letters, 236, 78-95.

Wade, J., Wood, B.J., and Tuff, J. (2012) Metal–silicate partitioning of Mo and W at high pressures and temperatures: Evidence for late accretion of sulphur to the Earth. Geochimica et Cosmochimica Acta, 85, 58-74.

Walter, M.J., Nakamura, E., Trønnes, R.G., and Frost, D.J. (2004) Experimental constraints on crystallization differentiation in a deep magma ocean. Geochimica et Cosmochimica Acta, 68(20), 4267-4284.

Welsch, B., Faure, F., Famin, V., Baronnet, A., and Bachèlery, P. (2012) Dendritic crystallization: a single process for all the textures of olivine in basalts? Journal of Petrology, 0, 1-36.

Wilke, M., Farges, F., Petit, P.E., Brown, J.G.E., and Martin, F. (2001) Oxidation state and coordination of Fe in minerals: An Fe K-XANES spectroscopic study. American Mineralogist, 86, 714-730.

Wood, B.J., and Rubie, D.C. (1996) The effect of alumina on phase transformations at the 660-kilometer discontinuity from Fe-Mg partitioning experiments. Science, 273, 1522-1524.

Xu, Y., McCammon, C.A., and Poe, B.T. (1998) The effect of alumina on the electrical conductivity of silicate perovskite. Science, 282, 922-924.

Figure captions

Figure 1 Example of XANES spectra measured on a bridgmanite of the sample #108 and the bridgmanite reference.

Figure 2 Comparison between iron pre-edge peaks fitted from the measurements performed using XANES on various Bg grains (dotted and dashed curves) and averaged pre-edge peaks (thick black curves). The vertical dotted lines show the energy position of the centroid.

Figure 3 Calibration for Fe^{3+}/Fe_{total} (%) as a function of the centroid position of the pre-edge (eV). The obtained calibration line (thick black line) from the standards (closed squares) agrees well within error with the working curve of Wilke et al. (2001) (dashed curve). The horizontal error bar on the andradite standard was obtained as the standard deviation of the measurements made on different directions of the andradite single crystal. It defines the upper and lower limits (dotted lines) for the calibration. The errors on the Fe^{3+} determination (standard deviations) on the samples (shown as open squares) are lower than that of andradite, which suggest a weak anisotropy in bridgmanite.

Figure 4 Backscattered electron images of samples #104 (**a-b**), #129 (**c**), #122 (**d**), #103 (**e**) and #108 (**f**). The samples are composed of liquid metal coexisting with bridgmanite (Bg), stishovite (st) and silicate melt (melt). The Al-free sample #122 is free of stishovite. Majorite (Maj) and liebermannite (K-hollandite) are present in sample #103 and sample #104 respectively. Bg1 and Bg2 stand for the first (Fe-poor, dark grey) and second (Fe-rich, light grey) Bg phases that crystallized upon cooling (see Supplementary Fig. 1 and text).

Figure 5 Change of the Fe, Al, Mg and Si partition coefficients between Bg and melt with the degree of partial melting. Full and open squares show partitioning coefficients derived from

the composition of Fe-poor (Bg1) and Fe-rich (Bg2) Bg phases, respectively. The coexisting melts are those observed in the sample directly (filled squares), or a reconstruction based on the phases that recrystallized from the primary liquid upon cooling (open squares) (see Supplementary Figure 1 and text for more details).

Figure 6 $Fe^{3+}/\Sigma Fe$ ratio of Bg as a function of Fe# and Al content (represented with colors) for the previous studies where iron metal is not present. The different symbols represent different redox conditions buffered through the capsule material and/or the composition of the sample (caps. = capsule, start= starting material, buff.= buffer). The triangles are samples containing Fe exclusively as Fe^{3+}. The colored lines are guidelines for different ranges of Al-contents (orange: Al=0.07 to 0.10 and green: Al=0.12 to 0.17) The plotted data are from (Frost and Langenhorst, 2002; Hummer and Fei, 2012; Lauterbach et al., 2000; McCammon et al., 2004; Saikia et al., 2009)..

Figure 7 Variations of the Fe^{3+}-pfu in bridgmanites for the present and previous studies where iron metal is present or not, as a function of the Fe/(Fe+Mg) ratio for Al-free (**a**) and both Al-free and Al-bearing samples (**b**). In (**a**), symbols correspond to experimental data while lines correspond to Fe^{3+}-pfu for relatively constant $Fe^{3+}/\Sigma Fe$ (indicated as numbers), where the Fe^{3+}pfu is calculated based on Equ. 3 (see text for more details). In (**b**), the lines are guidelines for constant Al-contents in Bg (red: Al=0.06 to 0.08 green: Al = 0.12 to 0.17). The symbols correspond to different redox conditions buffered through the capsule material and/or the composition of the sample (caps. = capsule, start= starting material, buff.= buffer). The triangles are samples containing Fe exclusively as Fe^{3+}. Colors represent in (**a**) various $Fe^{3+}/\Sigma Fe$ ratios and in (**b**) the Al content.

Figure 8 (**a**) $Fe^{3+}/\Sigma Fe$ ratio as a function of the average Al content in Bg of the present and previous studies (Frost and Langenhorst, 2002; Frost et al., 2004; Hummer and Fei, 2012;

Lauterbach et al., 2000; McCammon et al., 2004; Saikia et al., 2009; Terasaki et al., 2007). (**b**) Fe^{3+}-pfu as a function of the Al content where the Fe/(Fe+Mg) ratio is represented with colors. The colored curves are guidelines for different ranges of Fe/(Fe+Mg) (with colors same as symbols).

Figure 9 Schematic relation between the $Fe^{3+}/\Sigma Fe$ ratio and the fO_2 calculated for the samples of the present study and of Terasaki et al. (2007) and Frost et al. (2004). The relative fO_2 of the other studies was estimated from the capsule material and the use of Fe oxide exclusively as Fe_2O_3 powder buffer (see text for more details). The colored curves are guidelines for different ranges of Al-contents (with colors same as symbols). At the intermediate fO_2, when using Fe, Pt, Au or Re capsules, the guidelines are located at values extracted from the linear relationship between Al-content and $Fe^{3+}/\Sigma Fe$ (Eq.4 and Figure 10). Dashed curves for high Al-content are extrapolated guidelines following the trends for lower Al-content.

Figure 10 Correlation between $Fe^{3+}/\Sigma Fe$ ratio and Al-content in Bg for samples equilibrated in metal Fe, Re, Pt or Au capsules. The solid and dotted lines represent the linear fitted trend (Equ. 4) and the σ error of the linear regression.

Table 1 Experimental conditions and products.

Table 2 Results of the pre-edge fitting of standards and Bg unknowns and compositions of the analyzed Bg.

705   **Tables**

706   **Table 1** Chemical composition of the starting materials.

	EC-w/S-lSi	EC-w/S-hSi	EC-w/oS	EC-hAl-w/oS	EC-w/oAl-w/oS
Silicate					
SiO_2	62	62	62	60.4	62
TiO_2	0.21	0.21	0.21	0.2	0.21
Al_2O_3	2.6	2.6	2.6	5	0
Cr_2O_3	0.19	0.19	0.19	0.18	0.19
MgO	32.2	32.2	32.2	31.4	32.2
CaO	1.3	1.3	1.3	1.23	1.26
Na_2O	1.4	1.4	1.4	1.4	1.42
K_2O	0.14	0.14	0.14	0.14	0.14
MnO	0.04	0.04	0.04	0.04	0
Metal					
Fe	86.7	85.3	90.4	90.4	90.4
Ni	5.1	5	5.3	5.3	5.3
Si	1.5	3	2.5	2.5	2.5
Mn	0.88	0.87	0.91	0.91	0.91
Cr	0.65	0.64	0.68	0.68	0.68
Co	0.22	0.22	0.23	0.23	0.23
S	5	5	0	0	0

707   EC : Enstatite Chondrite ; w/S : S-bearing ; w/oS : S-free ; lSi : low Si metal content ; hSi : high
708   Si metal content; hAl : high Al content ; w/oAl : Al-free.

709

710   **Table 2** Experimental conditions and products.

Run	Temperature (°C)	Starting Material	Products	Time (min)	fO_2 (relative to IW)	Degree of melting*
#104	1900	EC-w/S-lSi	2 Bg - st - melt - Lieb - met	60	-2.06	1.5
#108	1900	EC-hAl-w/oS	2 Bg - st - melt -met	130	-1.93	6.1
#122	2050	EC-w/oAl-w/oS	Bg – melt - met	120	-2.01	69
#103	1900	EC-w/S-hSi	2 Bg- maj - st - melt -met	60	-1.73	8.7
#129	1900	EC-w/oS	2 Bg - st - melt - met	180	-1.49	6.1

* Degree of melting of the silicate phase, given in weight % and determined by mass balance calculations.

711

28

712 **Table 3** Results of the pre-edge fitting of standards and Bg unknowns and major elements concentrations in the analyzed Bg.

| | Sample | No. collected spectra | Total area | Centroid energy (eV) | Fe^{3+}/Fe (%) | Atoms per three oxygens | | | | | | $\Sigma Fe/(\Sigma Fe+Mg)$ |
						Mg	Fe^{2+}	Fe^{3+}	Al	Si	Total	
Standards	Andradite	4 different angles	0.079 (04)	7114.17 (16)	100							
	Siderite	4	0.066 (10)	7112.69 (06)	0							
	Bridgmanite*	8	0.110 (10)	7113.01 (05)	22							
	SC opx*	4	0.113 (09)	7112.85 (05)	5							
Bridgmanites	#104 Bg1	4	0.105 (04)	7112.92 (04)	14 ± 3	0.967	0.020	0.003	0.047	0.969	2.006	0.023
	#104 Bg2	1	0.167	7113.05	25	0.898	0.053	0.018	0.072	0.957	1.998	0.073
	#122	4	0.129 (03)	7113.02 (04)	22 ± 3	0.971	0.019	0.005	0.000	1.001	1.996	0.024
	#108 Bg1	5	0.136 (19)	7113.06 (10)	24 ± 6	0.939	0.012	0.004	0.113	0.937	2.005	0.017
	#129 Bg1	3	0.105 (04)	7112.97 (07)	18 ± 5	0.938	0.018	0.004	0.042	0.987	1.990	0.024
	#129 Bg2	2	0.105 (00)	7113.04 (05)	22 ± 4	0.935	0.033	0.009	0.053	0.970	1.999	0.043

[a] numbers in parenthesis are standard deviation of the total areas and the centroid energies.
* Standards measured by Mössbauer spectroscopy.

713

714

29

715   **Figures**

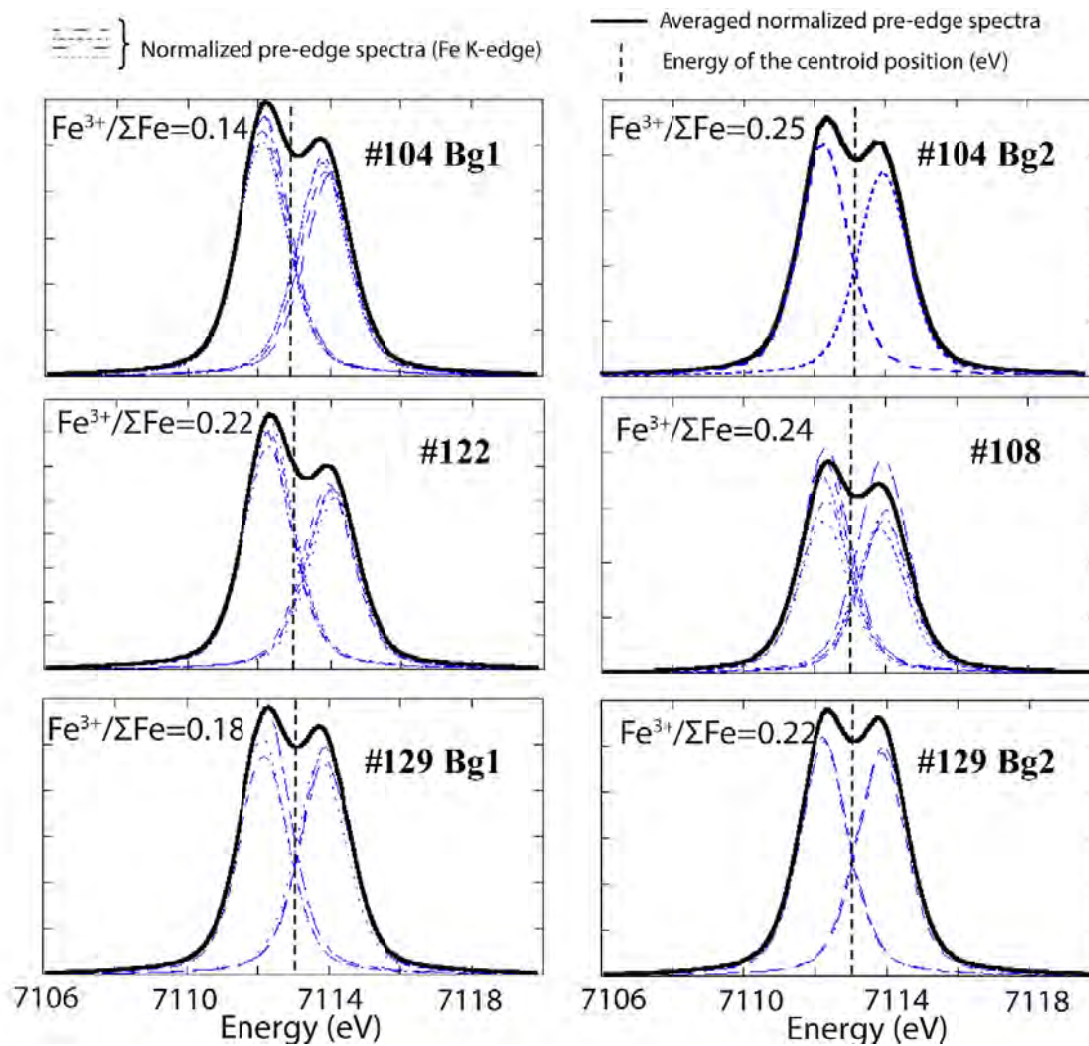716   **Figure 1**

717
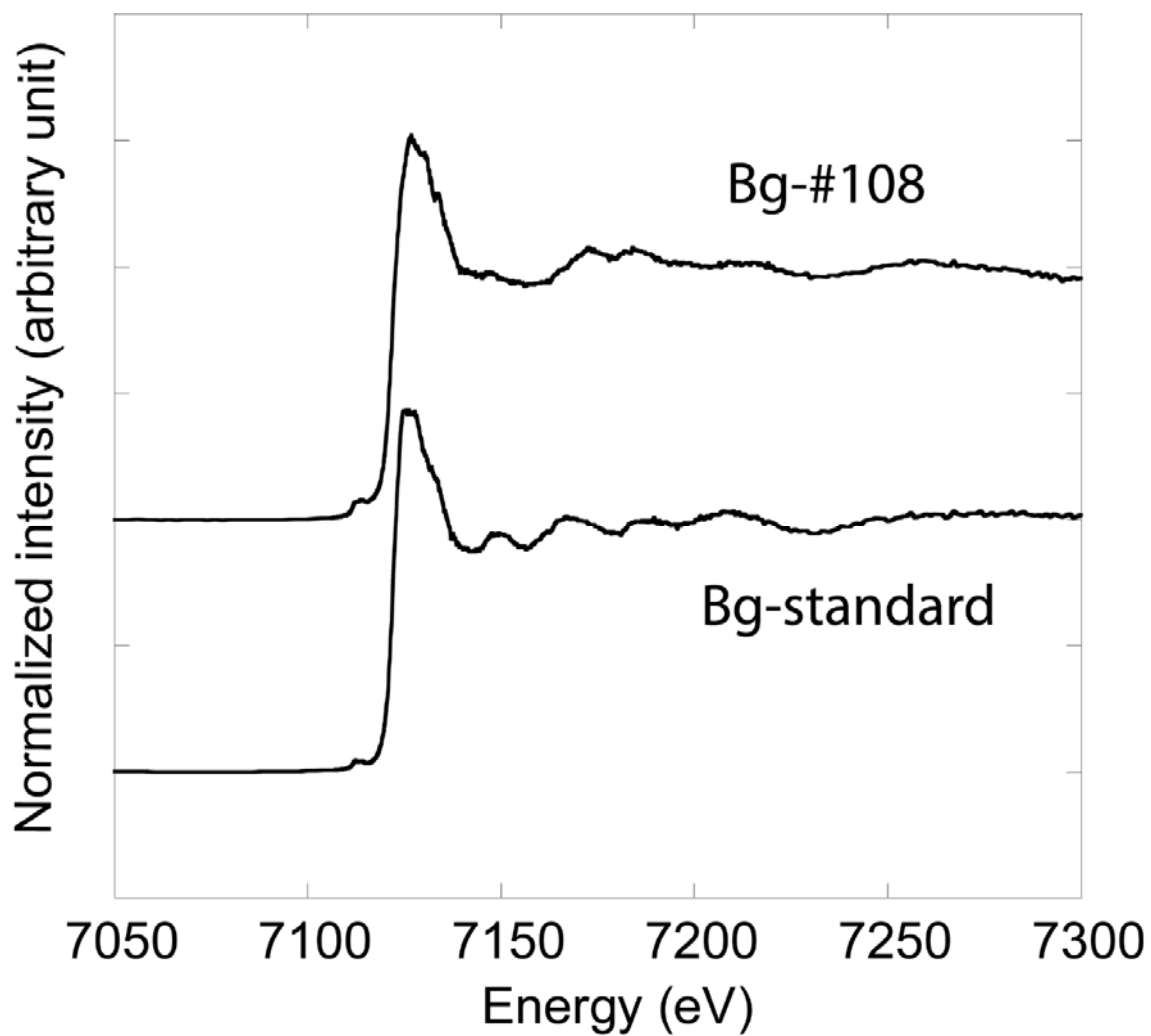
718
719
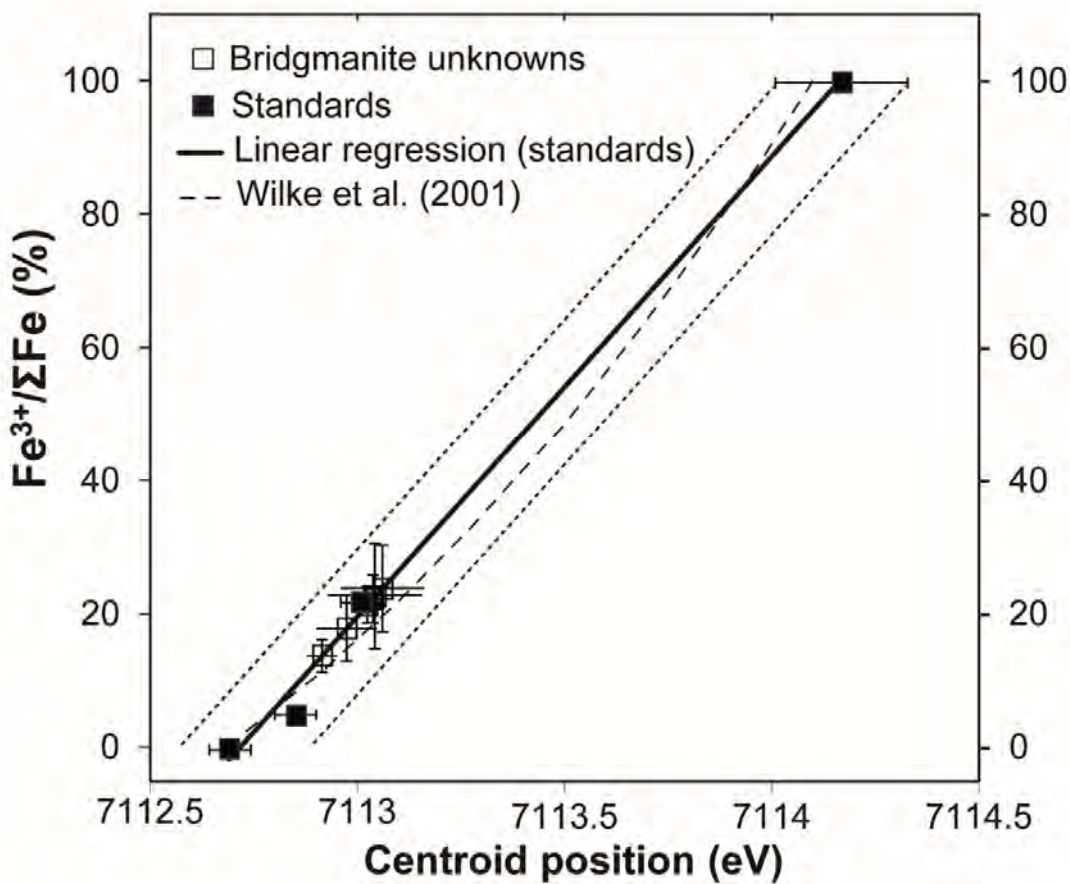720
721
722
723
724
725
726
727
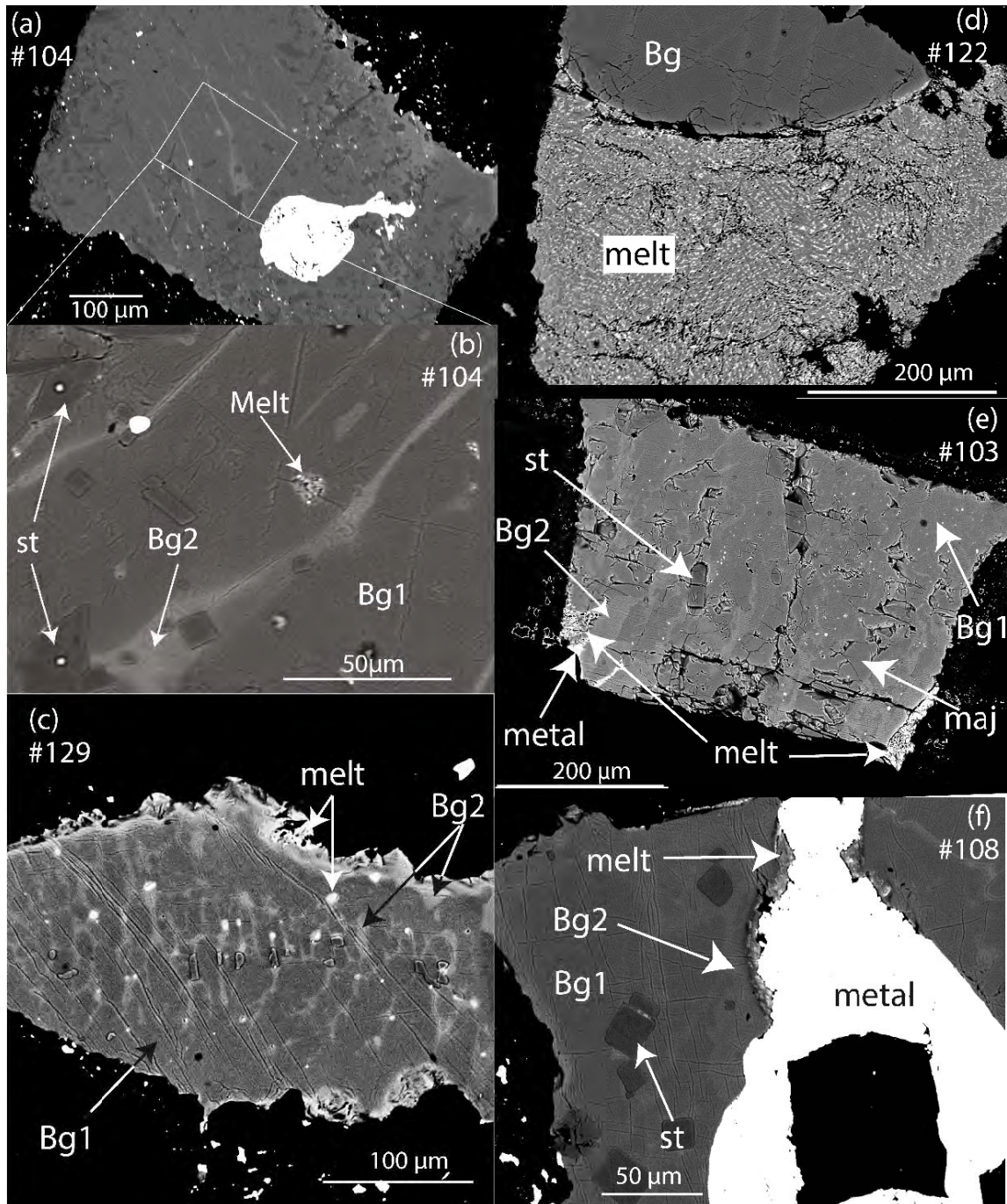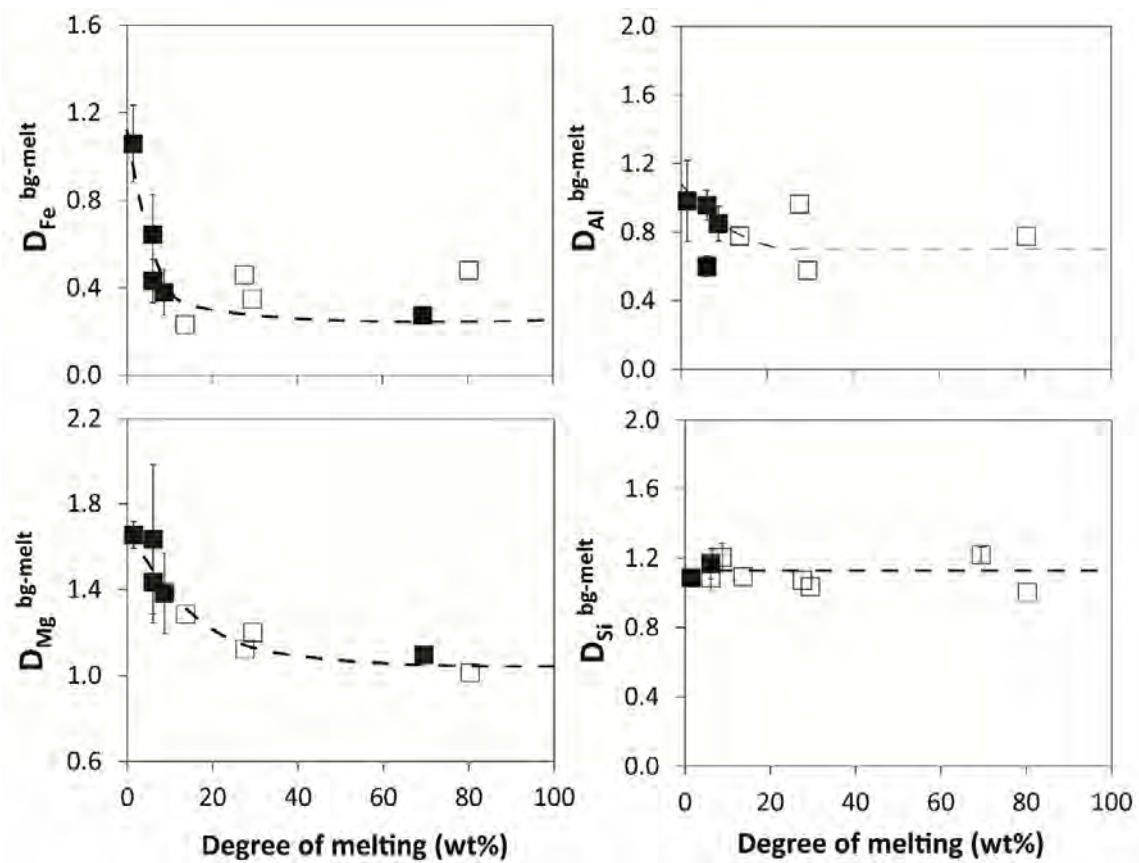
728   **Figure 2**

729

730

731   **Figure 3**

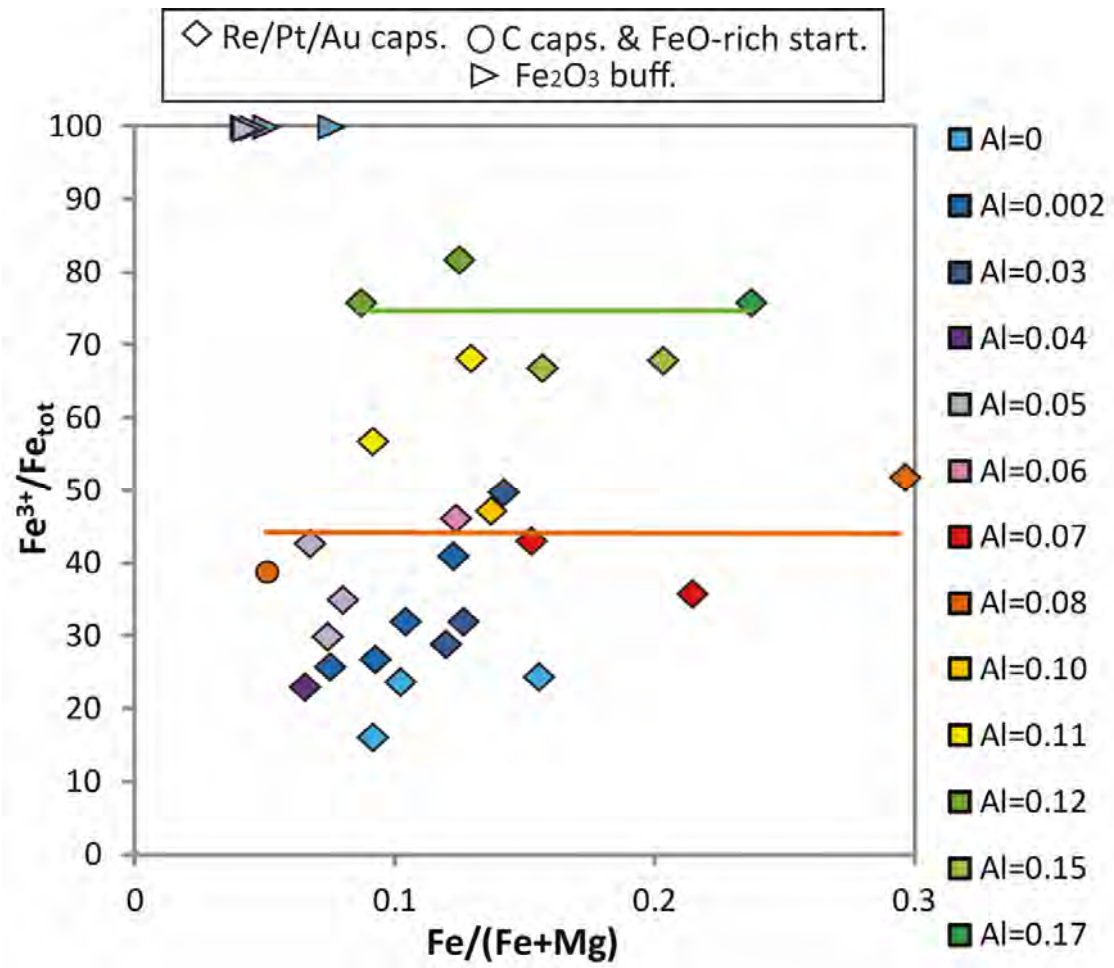732

733

734   **Figure 4**
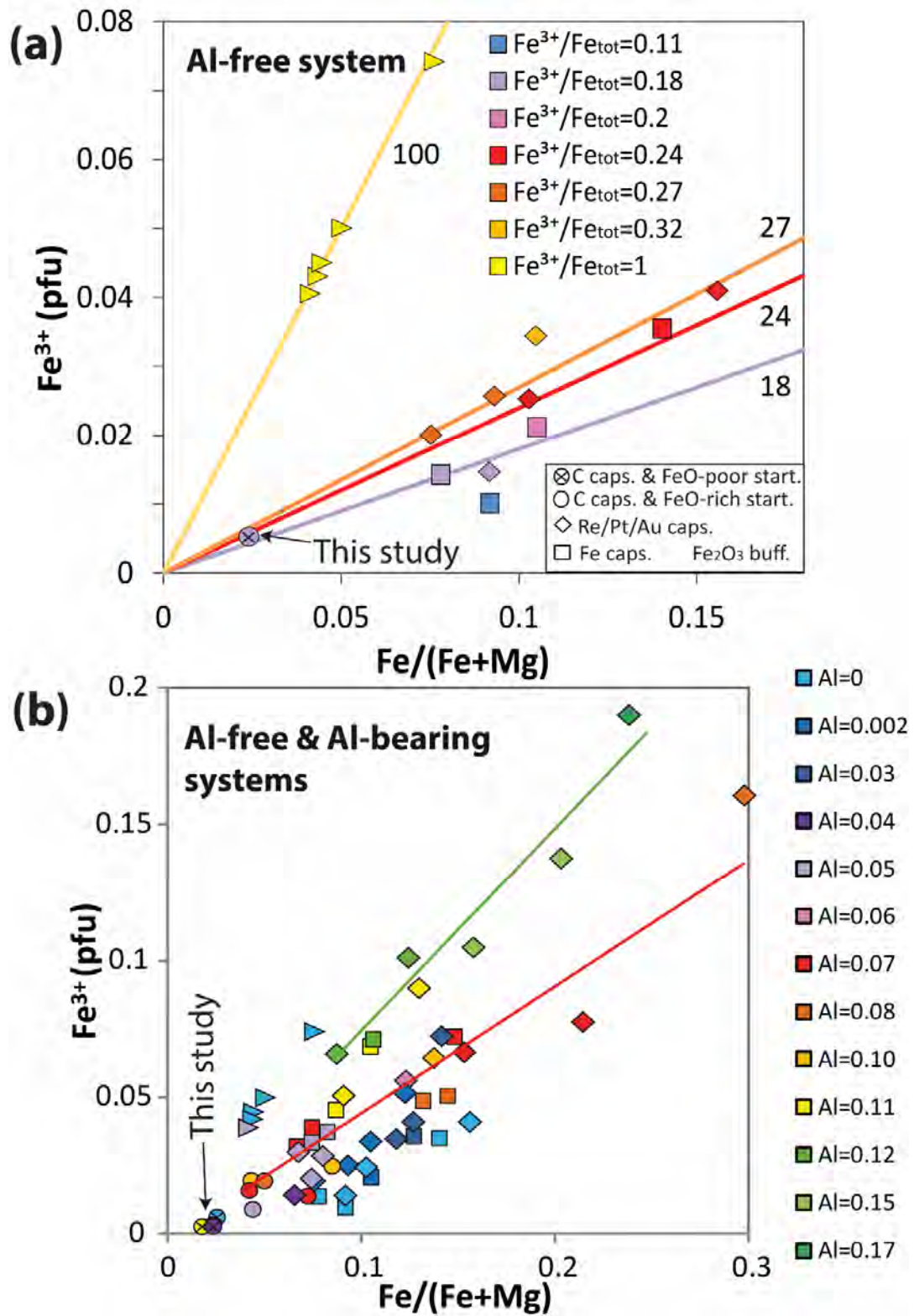

735

736

33

737   **Figure 5**

738

739

740   **Figure 6**
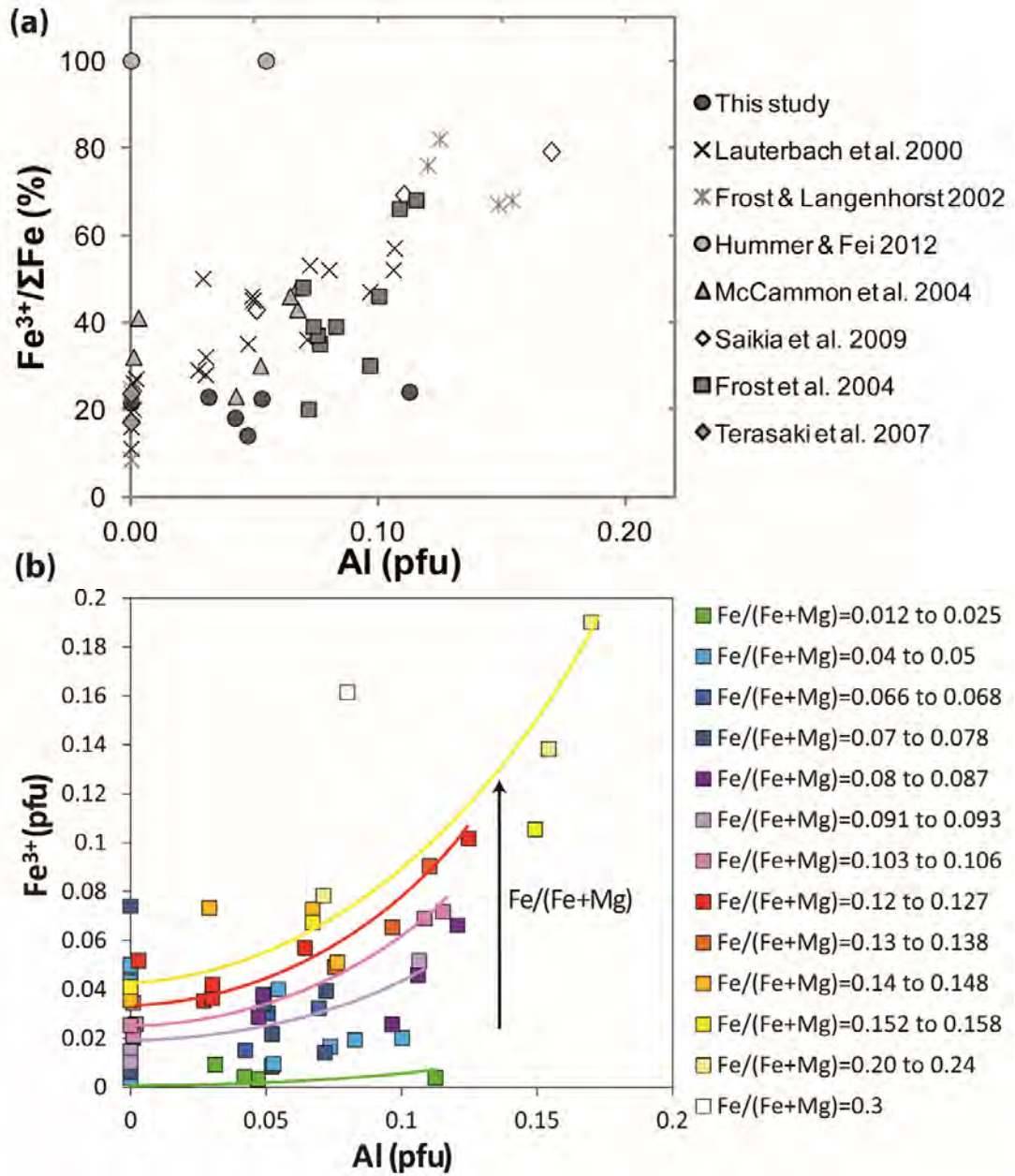

741

742

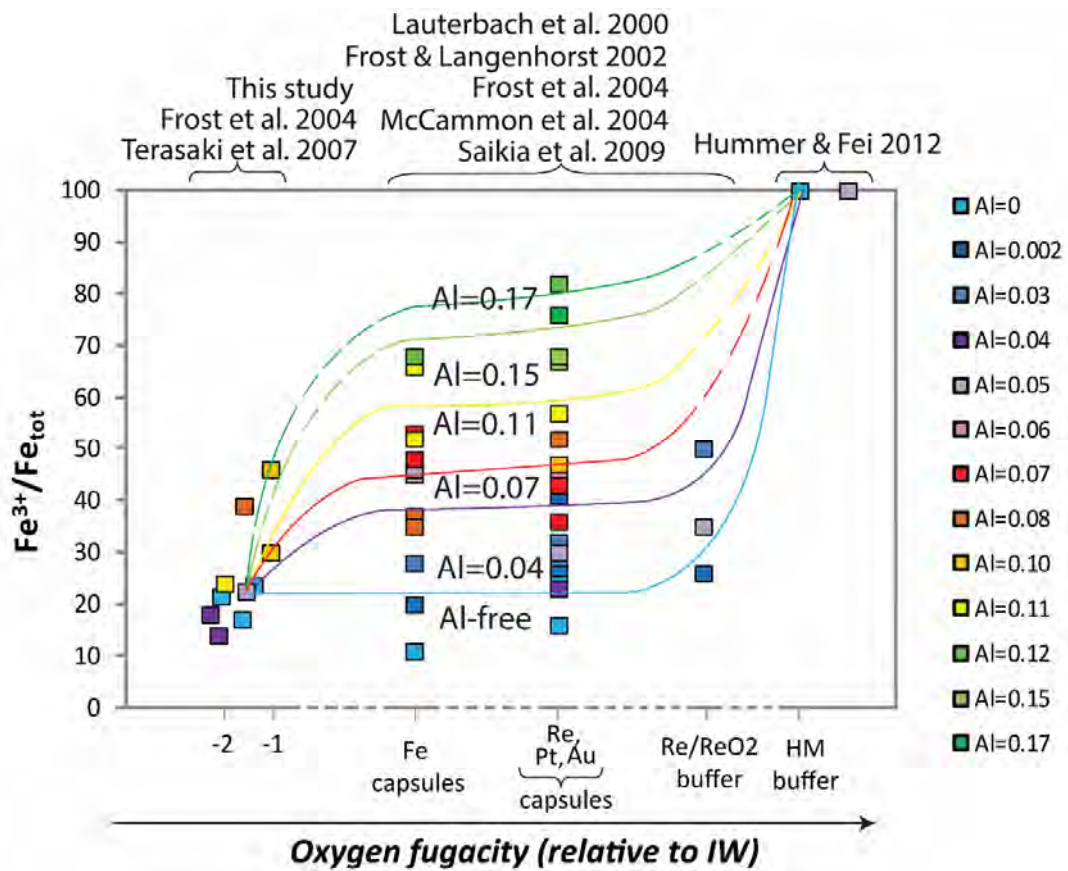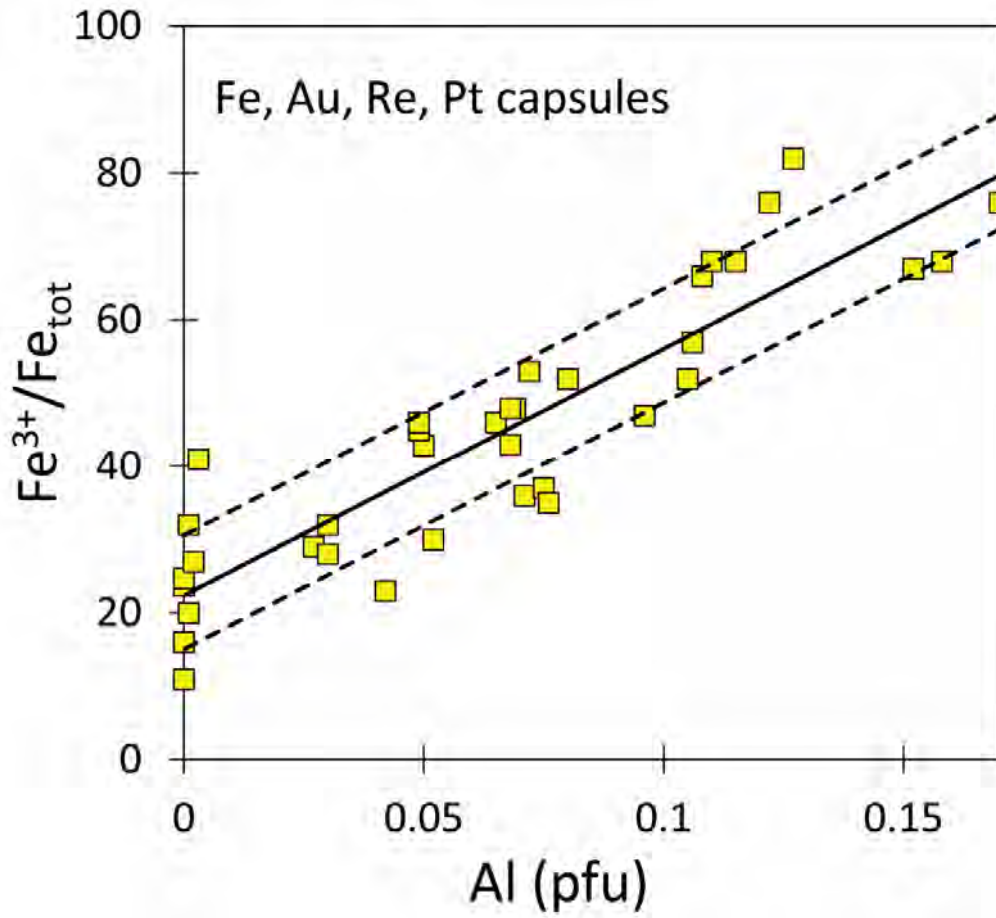743 **Figure 7**

744

745　　**Figure 8**

746

747

748   **Figure 9**

749

750

751   **Figure 10**

752

753

754

755